

---

# LEARNING FLUID-STRUCTURE INTERACTION DYNAMICS WITH PHYSICS-INFORMED NEURAL NETWORKS AND IMMERSED BOUNDARY METHODS

---

Afrah Farea<sup>1</sup>, Saiful Khan<sup>2</sup>, Reza Daryani<sup>1</sup>, Emre Cenk Ersan<sup>1</sup>, Mustafa Serdar Celebi<sup>1</sup>

<sup>1</sup>Computational Science and Engineering Department, Informatics Institute  
Istanbul Technical University, Istanbul 34469, Turkiye  
farea16@itu.edu.tr, daryani@itu.edu.tr, ersane@itu.edu.tr, mscelebi@itu.edu.tr

<sup>2</sup>Scientific Computing, Rutherford Appleton Laboratory  
Science and Technology Facilities Council (STFC), OX11 0QX, United Kingdom  
saiful.khan@stfc.ac.uk

We introduce neural network architectures that combine physics-informed neural networks (PINNs) with the immersed boundary method (IBM) to solve fluid-structure interaction (FSI) problems. Our approach features two distinct architectures: a Single-FSI network with a unified parameter space, and an innovative Eulerian-Lagrangian network that maintains separate parameter spaces for fluid and structure domains. We study each architecture using standard Tanh and adaptive B-spline activation functions. Empirical studies on a 2D cavity flow problem involving a moving solid structure show that the Eulerian-Lagrangian architecture performs significantly better. The adaptive B-spline activation further enhances accuracy by providing locality-aware representation near boundaries. While our methodology shows promising results in predicting the velocity field, pressure recovery remains challenging due to the absence of explicit force-coupling constraints in the current formulation. Our findings underscore the importance of domain-specific architectural design and adaptive activation functions for modeling FSI problems within the PINN framework.

## 1 Introduction

FSI problems, which involve the complex interplay between fluid and solid structures, are fundamental in computational engineering fields. The inherent complexity of FSI problems originates from the nonlinear dynamics occurring at fluid-solid interfaces, especially when involving deformable boundaries or turbulent flows. Traditional computational approaches to FSI involve coupling computational fluid dynamics (CFD) models with structural solvers. While these methods yield high-fidelity results, they are computationally intensive, especially in cases when resolving fine boundary movements and interfacial forces, making them impractical for large-scale or real-time applications.

IBM significantly addresses FSI computational complexity by efficiently coupling fluids with solid structures within a unified framework. Despite its flexibility, IBM has several limitations: (a) The sharp representation of the interface becomes blurred due to regularized delta functions, reducing accuracy near the fluid-solid boundary [1]. (b) Enforcing interfacial coupling conditions, e.g., no-slip and pressure continuity, can be challenging, particularly at high Reynolds numbers or significant structural deformations. (c) Numerical instability and convergence issues may arise when dealing with stiff materials or fine temporal resolutions [2]. (d) IBM formulations lack generalizability across different FSI scenarios, often requiring problem-specific tuning for varying geometries, material, and boundary conditions [3, 4]. These limitations highlight the need for improved frameworks that effectively learn and enforce interface conditions while maintaining computational efficiency.

Recent advancements in machine learning have introduced new methods for capturing complex fluid dynamics and structural responses with high computational efficiency [5, 6, 7, 8, 9, 10, 11, 12, 13]. PINNs offer a compelling approach by integrating observational data with governing physical laws to solve partial differential equations (PDEs). PINNs have been successfully applied to nonlinear dynamics [14, 15, 16, 17, 18]. Several studies have explored PINNs for FSI problems, showing promising results in predicting flow fields and structural responses. Integrating PINNs with IBM

has demonstrated the potential to combine the strengths of both approaches, enabling simple and efficient modeling without excessive computational overhead [19]. The IB-PINN frameworks [20, 21] apply penalty terms to enforce interface conditions but remain limited to stationary geometries and steady flows. More complex dynamics studies using operator learning and reduced-order models [7, 5] often lack explicit interface physics and require extensive training data. Moving boundary problems with region-specific loss partitioning and improved efficiency was proposed by [19], which still faces challenges with pressure recovery and sharp interface resolution.

These constraints highlight a lack of effective methods for capturing coupled dynamics in both moving and deforming environments, especially at the fluid-solid interface. Additionally, the lack of an existing dataset for simulating fluid-solid interactions and the absence of available source code hinder reproducibility and further research in this domain.

The problem of immersed-boundary fluid structure interaction resembles multi-task learning scenarios. In these scenarios, predicting multiple fields with distinct physical characteristics using a single architecture can lead to competing objectives due to parameter sharing [22, 23, 24, 25]. We propose that a locally-aware decoupled architecture may more effectively address the unique challenges associated with immersed-boundary fluid structure interaction problems. To achieve this, we propose:

A **decoupled architecture** that separates a feed-forward neural network into two specialized networks: one for the Eulerian fluid domain and another for the Lagrangian solid interface. This innovative approach is referred to as the Eulerian-Lagrangian architecture throughout the remainder of the paper. By distinguishing between these architectures, we enable each network to focus on its specific domain, which reduces interference and enhances learning efficiency. To evaluate the effectiveness of this architecture with a Single-FSI architecture that employs a unified network to predict both fluid flow variables at the fluid and solid interfaces.

Additionally, we incorporate a **locality-aware representation** into these neural network architectures that leverages the principles of IBM. This is achieved through adaptive B-spline activation, which provides local control and improves the capture of high-gradient features near fluid-solid interfaces. This method aligns seamlessly with IBM’s strategy for managing sharp interface dynamics through localized forcing and smoothing functions.

Consequently, we develop four models by implementing each network architecture, e.g., Single-FSI and Eulerian-Lagrangian, with the two activation function schemes, e.g., standard Tanh and adaptive B-spline basis function. We trained and evaluated the models using a dataset generated from a simulation featuring a moving object modeled by IBM, as explained in [4]. We verified the simulation against high-precision numerical solutions obtained from the Immersed Boundary Method Adaptive Mesh Refinement (IBAMR) simulation software [26]. The dataset, source code, and pre-trained models from this study are publicly available at [https://github.com/afrah/pinn\\_fsi\\_ibm](https://github.com/afrah/pinn_fsi_ibm) to ensure reproducibility and facilitate further exploration of the IB-FSI problem.

## 2 Related Work

Recent years have seen growing interest in leveraging neural networks to solve FSI problems, particularly through the integration of Physics-Informed machine learning approaches with immersed boundary techniques. Fang et al.[20] developed an immersed boundary–PINN (IB-PINN) framework for fluid-solid coupling, demonstrating promising results in modeling 2D flow past a static cylinder. Their model, however, was restricted to stationary solid boundaries for the entire domain. Similarly, Huang et al.[21] proposed a direct-forcing immersed boundary PINN that introduced velocity and force penalty terms to enforce interface conditions. Although effective for steady flows around fixed geometries, their formulation does not support deforming or moving structures. Xiao et al. [7] employed a Fourier Neural Operator-based approach to predict vesicle dynamics in fluids, offering efficiency in long-term dynamics and parameter generalization. Nevertheless, their operator learning approach lacks a physics-constrained enforcement of interfacial conditions and is less suited for tasks requiring high-fidelity resolution of boundary dynamics.

Han et al.[5] introduced a neural network-based reduced-order model (ROM) for vortex-induced vibration (VIV) problems. While reduced-order models offer efficient surrogate approximations, they require extensive precomputed high-fidelity data and lack the physics-consistency and flexibility of PINNs in extrapolating to new scenarios or partial observations. Sundar et al.[19] explored PINN-based frameworks for moving boundary problems by proposing two variants: MB-PINN, which considers only the fluid region, and MB-IBM-PINN, which includes both fluid and solid regions. They investigated relaxation of physics constraints and region-specific loss weighting to improve accuracy and generalization. Furthermore, they highlight challenges in training PINNs for moving boundary problems, particularly regarding pressure recovery and the accurate resolution of localized flow features.

Table 1: Statistical summary for FSI-IBM model problem with velocity and pressure values.

Domain	Field	Standard Deviation	Distribution
Fluid	$u$	0.208	
	$v$	0.130	
	$p$	0.115	
Solid	$u$	0.121	
	$v$	0.106	
	$p$	0.085	
Solid Interface	$u$	0.145	
	$v$	0.133	
	$p$	0.181	

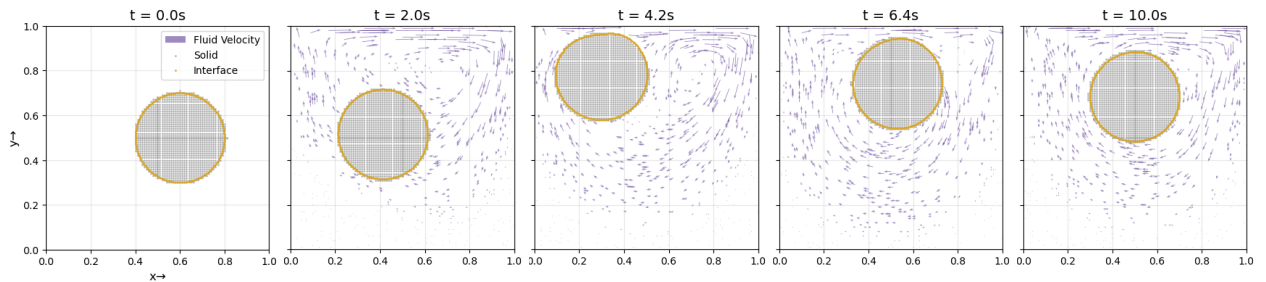


Figure 1: Illustration of the computational domain of the FSI problem showing the movement of a soft disc in a lid-driven cavity flow at different time steps.

### 3 FSI with IBM

The FSI problem involves the dynamic interaction between fluid and solid structures. This interaction is complex because changes in one domain, such as the fluid or solid, directly affect the other, creating a feedback loop. For example, when a fluid flows around a flexible structure, it exerts forces that cause the structure to deform. This deformation, in turn, alters the fluid flow, leading to changes in the forces acting on the structure.

Because FSI problems are highly complex, a variety of numerical strategies have been developed. These include body-fitted, mesh-conforming schemes such as ALE finite-element/finite-volume methods, as well as non-body-conforming approaches like the immersed-boundary or fictitious-domain methods. Mesh-free particle techniques and reduced-order models are also used in specialised contexts.

FSI methods are generally categorized as body-conforming or non-body-conforming, depending on whether the fluid mesh conforms to the structure. This classification is independent of whether the structure is elastic or rigid. IBM is a non-body conforming method in which the fluid domain mesh does not require frequent mesh generation during the deformation of the structure. That is, it uses a static Cartesian mesh for the fluid part and curvilinear Lagrangian nodes for the structure domain, where it can freely move over the background mesh. This property enables this method to be inherently suitable for significant displacement problems, such as modelling biological valves like an aortic valve [27]. In this method, the continuity, momentum, and incompressibility of the fluid domain are described using the Eulerian approach, while the deformation, stresses, and forces on the structure are described in a Lagrangian manner. Eulerian and Lagrangian variables are coupled using integral transforms with delta kernel functions.

### 3.1 Problem Setup

This study examines an FSI scenario involving a circular elastic solid object within a fluid, using a direct forcing IBM. Following the setup described in [4], we model the fluid as a time-dependent, two-dimensional cavity flow discretized using the finite difference method. Lagrangian marker points represent the solid boundary, while the solid domain is discretized with the finite element method, enforcing no-slip boundary conditions at the solid boundary.

The computation domain, denoted as  $\Omega$ , is a two-dimensional square cavity defined by  $\Omega = [0, 1] \times [0, 1]$ . The immersed structure is a disc with a radius of 0.2, initially centered at the point  $\mathbf{x} = (0.6, 0.5)$ . We consider a uniform discretization with a grid  $(N_x, N_y) = (100, 100)$  and a time span  $0 \leq t \leq 10$ , with a time step of 0.01. During this interval, the disc completes slightly more than one full rotation within the cavity. The boundary  $\Gamma_1$  represents the top Dirichlet boundary condition of the cavity with velocity tangent to this side, while  $\Gamma_0$  denotes the other three stationary sides. The Reynolds number of the flow is set to  $Re = 100$ . During the simulation, the flow induced by the driven lid causes the structure to come nearly into contact with the moving upper boundary of the domain, as illustrated in Fig. 1.

The governing equations for the fluid domain consist of the incompressible Navier-Stokes equations along with appropriate boundary and interface conditions that couple the motion of the fluid and the solid interface as follows:

#### Fluid Dynamics: Navier-Stokes Equations

$$\rho_f \left( \frac{\partial \mathbf{u}_f(t, \mathbf{x})}{\partial t} + \mathbf{u}_f(t, \mathbf{x}) \cdot \nabla \mathbf{u}_f(t, \mathbf{x}) \right) = -\nabla p_f(\mathbf{x}, t) + \mu_f \nabla^2 \mathbf{u}_f(t, \mathbf{x}) + \mathbf{f}_{\text{ext}}(\mathbf{x}, t), \quad \text{in } \Omega_f \quad (1a)$$

$$\begin{aligned} \nabla \cdot \mathbf{u}_f(t, \mathbf{x}) &= 0, & \text{in } \Omega_f \\ \mathbf{u}(0, \mathbf{x}) &= 0, & \text{in } \Omega \\ \mathbf{u}(t, \mathbf{x}_0) &= 0, & \text{in } \Gamma_i \\ \mathbf{u}(t, \mathbf{x}_1) &= 1, & \text{in } \Gamma_0 \end{aligned}$$

#### Coupling Equations (Interface Condition):

$$\frac{\partial \mathbf{d}_s(\xi(t, s))}{\partial t} = \mathbf{u}_s(\xi(t, s)) = \int_{\Omega} \mathbf{u}_f(t, \mathbf{x}) \delta(\mathbf{x} - \xi(t, s)) d\mathbf{x} = \mathbf{u}_f(\xi(t, s)), \quad (1b)$$

$$\nabla p(\xi(t, s)) \cdot \mathbf{n} = 0 \quad (1c)$$

where  $f_{\text{ext}}$  represents the source term,  $p_f$  is a scalar pressure field,  $\mathbf{f}_{\text{Eulerian}}(t, \mathbf{x})$  is the Eulerian elastic force density exerted by the solid on the fluid and distributed using the immersed boundary method.  $\mathbf{f}_{\text{Lagrangian}}$  is the Lagrangian elastic force density added to the solid interface.  $\mathbf{u}(t, \mathbf{x}) = (u(t, x), v(t, y))$  is the velocity field where  $\mathbf{x} = (x, y)$ ,  $\xi(t, s)$  is the embedded solid interface representing the Lagrangian points,  $\mu_f$  is the dynamic viscosity of the fluid such that  $\mu_f = \frac{1.0}{Re} = 0.01$ , with  $Re$  as the Reynold number,  $\rho_f$  represents the fluid density, set to unity.

The coupling conditions in Eq. 1b are fundamental to the IBM method, facilitating the interaction between the fluid and solid domains in FSI problems. Specifically, Eq. 1b enforces the no-slip boundary condition by ensuring that the fluid velocity at the interface,  $\xi(s, t)$ , matches the velocity of the solid structure.

While this formulation effectively captures the essential fluid-interface dynamics, it simplifies the full FSI problem by treating the solid mainly as a moving interface without modeling its internal dynamics (e.g., elasticity, stress, mass) and not learning the interface force balance equations. As a result, this simplification allows us to demonstrate the core methodology while recognizing that future work should incorporate force exchange conditions (and perhaps structural PDEs) to improve physical fidelity and predictive robustness.

The data in Table 1 highlight the statistical distribution of the target variables, including velocity and pressure values for different domains: Eulerian Fluid, Solid, and the Solid Lagrangian Interface. The table shows the standard deviation (Std) and the distribution of each component. The Eulerian domain has relatively low standard deviations for velocity and pressure components, suggesting that these quantities are generally smooth and continuous within these regions.

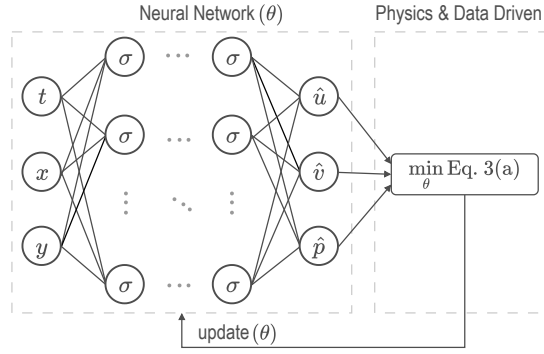


Figure 2: Single-FSI PINN network: the input variables are  $\{t, x, y\}$  (from both Eulerian and Lagrangian domains) and the output variables are  $\{\hat{u}, \hat{v}, \hat{p}\}$  for velocity components and the pressure (for both Eulerian and Lagrangian) respectively. For activation ( $\sigma$ ), we used both Tanh and B-spline.

## 4 Proposed Neural Networks

In FSI problems, the design of the loss function in PINNs is particularly important since it needs to incorporate multiple terms that represent the governing equations, coupling conditions, and boundary constraints. The complexity of FSI systems, with their intricate boundary conditions, requires carefully balancing the loss function terms. Additionally, effective loss weighting values (denoted as  $\lambda_k$ ) are essential to appropriately balance the contributions from each term, ensuring that the network does not overly prioritize one loss term at the expense of others. As a result, the careful design of the loss function and the weighting strategy is crucial for accurately modeling FSI behavior, where precise adherence to boundary conditions and coupling dynamics is fundamental for achieving a realistic solution.

The loss function  $\mathcal{L}$  in PINN combines terms for the governing equations and boundary conditions that need to be minimized. More formally:

$$\mathcal{L}(\theta) = \arg \min_{\theta} \sum_{k=1}^n \lambda_k \mathcal{L}_k(\theta) = \arg \min_{\theta} \left( \lambda_1 \mathcal{L}(D[u(x); a] - f(x)) + \sum_{k=2}^{n_f} \lambda_k \mathcal{L}(B[u(x)] - g_k(x)) \right) \quad (2)$$

where  $n$  is the total number of loss terms,  $\lambda_k$  is the weighting coefficient for each respective loss term, and  $\theta$  denotes the trainable parameters. Here,  $B[u(x)]$ ,  $D[u(x); a]$ , represent the boundary conditions and differential operators on the neural network output  $u(x)$ , enforcing physical constraints such as continuity and momentum conservation. A key observation about this approach is that the loss function is multi-objective, potentially incorporating terms with different physical scales. This variation can affect both convergence and the quality of the solution [28, 29]. Therefore, creating a PINN model to solve Eq. 1 involves leveraging neural networks to approximate the solution of the Navier-Stokes equations for the fluid domain while enforcing the boundary conditions as part of the training process.

We examined two neural networks with two neural network models: a standard MLP with a Tanh activation function and a KAN with a B-splines basis function. In the following subsections, we discuss the proposed network, the (hyper)parameter settings, and the loss function design used for training.

### 4.1 Single-FSI Network

In this network, shown in Fig. 2, a single feedforward neural network is used. The input variables are  $\{t, x, y\}$  from both Eulerian and Lagrangian domains, and the output variables are  $\{\hat{u}, \hat{v}, \hat{p}\}$  for velocity components and the pressure values, respectively.

The overall loss function  $L(\theta)$  comprises multiple terms that enforce the fluid's governing equations, boundary conditions terms according to the IBM approach as follows:

$$\mathcal{L}(\theta) = \lambda_1 \|\mathcal{L}_{\text{phy}}^{\text{fluid}}\|_{\Omega_f} + \lambda_2 (\|\mathcal{L}_{\text{up}}\|_{\Gamma_1} + \|\mathcal{L}_{\text{bc}_1}\|_{\Gamma_0}) + \lambda_3 \|\mathcal{L}_0\|_{\Omega_0} + \lambda_4 \|\mathcal{L}_{\xi}\|_{\xi}, \quad (3a)$$

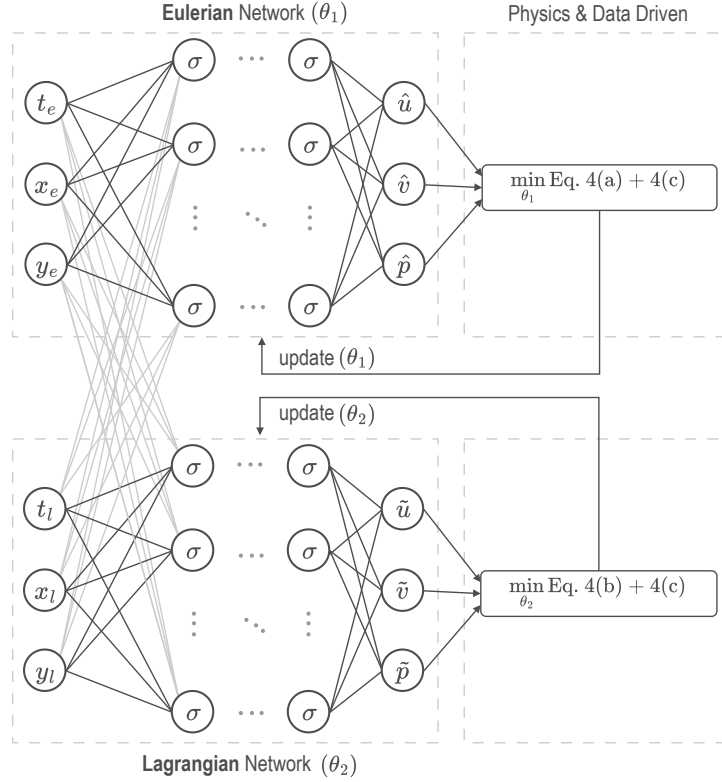


Figure 3: Eulerian-Lagrangian network: the inputs of the Eulerian Network ( $\theta_1$ ) are  $\{t_e, x_e, y_e\}$  from the Eulerian fluid domain, and the output variables are  $\{\hat{u}, \hat{v}, \hat{p}\}$  representing the Eulerian velocity and pressure fields respectively. For the Lagrangian Network ( $\theta_2$ ), the input variables are  $\{t_l, x_l, y_l\}$  representing the Lagrangian solid interface and the output variables are  $\{\tilde{u}, \tilde{v}, \tilde{p}\}$  representing the Lagrangian velocity and pressure values respectively.

where  $\mathcal{L}_{\text{phy}}^{\text{fluid}} = \mathcal{L}_{r_u}^{\text{fluid}} + \mathcal{L}_{r_v}^{\text{fluid}} + \mathcal{L}_{r_c}^{\text{fluid}}$ . We select 0.1, 2.0, 4.0, 0.1 for  $\lambda_1, \lambda_2, \lambda_3, \lambda_4$  respectively such that.

$$\mathcal{L}_{r_u}^{\text{fluid}}(\theta) = \text{MSE} \left[ \frac{\partial \hat{u}}{\partial t} + \hat{u} \frac{\partial \hat{u}}{\partial x} + \hat{v} \frac{\partial \hat{u}}{\partial y} + \frac{1.0}{\rho_f} \frac{\partial \hat{p}}{\partial x} - \mu \left( \frac{\partial^2 \hat{u}}{\partial x^2} + \frac{\partial^2 \hat{u}}{\partial y^2} \right) \right], \quad (3b)$$

$$\mathcal{L}_{r_v}^{\text{fluid}}(\theta) = \text{MSE} \left[ \frac{\partial \hat{v}}{\partial t} + \hat{u} \frac{\partial \hat{v}}{\partial x} + \hat{v} \frac{\partial \hat{v}}{\partial y} + \frac{1.0}{\rho_f} \frac{\partial \hat{p}}{\partial y} - \mu \left( \frac{\partial^2 \hat{v}}{\partial x^2} + \frac{\partial^2 \hat{v}}{\partial y^2} \right) \right], \quad (3c)$$

$$\mathcal{L}_{r_c}^{\text{fluid}}(\theta) = \text{MSE} \left[ \frac{\partial \hat{u}}{\partial x} + \frac{\partial \hat{v}}{\partial y} \right], \quad (3d)$$

$$\mathcal{L}_{\text{up}}(\theta) = \text{MSE} [1.0 - \hat{u}] + \text{MSE} [\hat{v}], \quad (3e)$$

$$\mathcal{L}_{\text{bc}_1}(\theta) = \mathcal{L}_{\text{bottom, right, left}} = \text{MSE} [\mathcal{L}(\hat{u}) + \mathcal{L}(\hat{v})], \quad (3f)$$

$$\mathcal{L}_0(\theta) = \text{MSE} [\hat{u} + \hat{v} + \hat{p}], \quad (3g)$$

$$\mathcal{L}_{\xi}(\theta) = \text{MSE} [\hat{u} - \hat{u}(\xi(s, t))] + \text{MSE} [\hat{v} - \hat{v}(\xi(s, t))] + \text{MSE} \left[ \frac{\partial \hat{p}(\xi(s, t))}{\partial n} \right], \quad (3h)$$

where,  $\mathcal{L}_{\text{phy}}^{\text{fluid}}$ ,  $\mathcal{L}_s$  are the losses of the fluid and solid interface, respectively.  $\mathcal{L}_{\text{left}}$ ,  $\mathcal{L}_{\text{right}}$ ,  $\mathcal{L}_{\text{up}}$ ,  $\mathcal{L}_{\text{bottom}}$ ,  $\mathcal{L}_{u_0}$ , are the left, right, up, bottom and initial losses respectively.

Table 2: Implemented models based on the proposed networks in Fig. 2 and Fig. 3, and their configurations are considered for evaluation in this work.

Model	Network	Structure	#Parameters	Activation
M1	Single-FSI (Fig. 2)	[3, 300, 300, 300, 3]	183305	Tanh
M2		[3, 100, 100, 100, 3]	208000	B-splines
M3	Eulerian-Lagrangian (Fig. 3)	Eulerian [3, 300, 300, 300, 3]	365105	Tanh
		Lagrangian [3, 300, 300, 300, 3]		
M4	Eulerian-Lagrangian (Fig. 3)	Eulerian [3, 100, 100, 100, 3]	411000	B-splines
		Lagrangian [3, 100, 100, 100, 3]		

## 4.2 Eulerian-Lagrangian Network

Eulerian-Lagrangian architecture is a decoupled neural network where the Eulerian Fluid Network ( $\theta_1$ ) is on the Eulerian domain and the Lagrangian Interface Network ( $\theta_2$ ) focuses on the Lagrangian interface domain. The inputs of the Eulerian Fluid Network ( $\theta_1$ ) are  $\{t_e, x_e, y_e\}$  from the Eulerian fluid domain and the output variables are  $\{\hat{u}, \hat{v}, \hat{p}$  representing the Eulerian velocity and pressure values. The input variables for the Lagrangian Interface network ( $\theta_2$ ) are  $\{t_l, x_l, y_l\}$  representing the Lagrangian solid interface temporal and spatial coordinates. The output variables are  $\{\tilde{u}, \tilde{v}, \tilde{p}\}$ , representing the Lagrangian velocity and pressure values, respectively.

The loss function considered in this model combines the PDE residuals, coupling, and boundary conditions as follows:

$$\mathcal{L}(\theta_1) = \lambda_5 \|\mathcal{L}_{\text{phy}}^{\text{fluid}}\|_{\Omega_f} + \lambda_1 (\|\mathcal{L}_{\text{up}}\|_{\Gamma_1} + \|\mathcal{L}_{\text{bc}_1}\|_{\Gamma_0}) + \lambda_2 \|\mathcal{L}_{u_0}\|_{\Omega}, \quad (4a)$$

$$\mathcal{L}(\theta_2) = \lambda_3 \mathcal{L}_s \quad (4b)$$

$$\mathcal{L}(\theta_1 \cup \theta_2) = \lambda_6 \mathcal{L}_\xi \quad (4c)$$

where  $\mathcal{L}_{\text{phy}}^{\text{fluid}} = \mathcal{L}_{r_u}^{\text{fluid}} + \mathcal{L}_{r_v}^{\text{fluid}} + \mathcal{L}_{r_c}^{\text{fluid}}$ . We select 2.0, 2.0, 2.0, 0.2, 0.1, 0.2 for  $\lambda_1, \lambda_2, \lambda_3, \lambda_4, \lambda_5, \lambda_6$  respectively such that.

$$\mathcal{L}_{\text{up}}(\theta_1) = \text{MSE}[1.0 - \hat{u}] + \text{MSE}[\hat{v}], \quad (4d)$$

$$\mathcal{L}_{\text{bc}_1}(\theta_1) = \mathcal{L}_{\text{bottom, right, left}} = \text{MSE}[\mathcal{L}(\hat{u}) + \mathcal{L}(\hat{v})], \quad (4e)$$

$$\mathcal{L}_{u_0}(\theta_1) = \text{MSE}[\hat{u} + \hat{v} + \hat{p}], \quad (4f)$$

$$\mathcal{L}_{r_c}^{\text{fluid}}(\theta_1) = \text{MSE}\left[\frac{\partial \hat{u}}{\partial x} + \frac{\partial \hat{v}}{\partial y}\right], \quad (4g)$$

$$\mathcal{L}_{r_u}^{\text{fluid}}(\theta_1) = \text{MSE}\left[\frac{\partial \hat{u}}{\partial t} + \hat{u} \frac{\partial \hat{u}}{\partial x} + \hat{v} \frac{\partial \hat{u}}{\partial y} + \frac{1.0}{\rho_f} \frac{\partial \hat{p}}{\partial x} - \mu \left(\frac{\partial^2 \hat{u}}{\partial x^2} + \frac{\partial^2 \hat{u}}{\partial y^2}\right)\right], \quad (4h)$$

$$\mathcal{L}_{r_v}^{\text{fluid}}(\theta_1) = \text{MSE}\left[\frac{\partial \hat{v}}{\partial t} + \hat{u} \frac{\partial \hat{v}}{\partial x} + \hat{v} \frac{\partial \hat{v}}{\partial y} + \frac{1.0}{\rho_f} \frac{\partial \hat{p}}{\partial y} - \mu \left(\frac{\partial^2 \hat{v}}{\partial x^2} + \frac{\partial^2 \hat{v}}{\partial y^2}\right)\right], \quad (4i)$$

$$\mathcal{L}_\xi(\theta_1 \cup \theta_2) = \text{MSE}[\hat{u}(\xi(s, t)) - \tilde{u}(\xi(s, t))] + \text{MSE}[\hat{v}(\xi(s, t)) - \tilde{v}(\xi(s, t))], \quad (4j)$$

$$\mathcal{L}_s(\theta_2) = \text{MSE}\left[\frac{\partial \tilde{p}(\xi(s, t))}{\partial n}\right]$$

where,  $\mathcal{L}_{\text{phy}}^{\text{fluid}}$ ,  $\mathcal{L}_s$  are the losses of the fluid and the solid interface, respectively.  $\mathcal{L}_{\text{left}}$ ,  $\mathcal{L}_{\text{right}}$ ,  $\mathcal{L}_{\text{up}}$ ,  $\mathcal{L}_{\text{bottom, right}}$ ,  $\mathcal{L}_{u_0}$ , are the left, right, up, bottom and initial losses respectively. In Eq. 4j,  $\hat{u}, \hat{v}$  represent the predicted velocity components from the Eulerian (fluid) network at the interface while  $\tilde{u}, \tilde{v}$  are the velocity components predicted by the Lagrangian (interface) network at the same points. This term penalizes any differences between the predicted fluid and interface velocities, enforcing a no-slip boundary condition at the interface.

## 4.3 Model Details

Based on the proposed networks, Single-FSI (Fig. 2) and Eulerian-Lagrangian (Fig. 3), we developed four models with various configurations as summarized in Table 2. With each network, we used varying structures: (a) [3, 100, 100, 100, 3] and (b) relatively deeper [3, 300, 300, 300, 3]; and activation functions: (a) standard Tanh and, (b) adaptive B-splines.

The Tanh-activated configurations are implemented as an MLP. These models adopt a fully connected feedforward network, where each layer is initialized using the Xavier normal distribution to ensure stable gradients during training.

The model normalizes inputs to the range  $[-1, 1]$ , to enhance training stability when using tanh activations. In contrast, the learnable B-spline basis functions for activation are implemented using the Kolmogorov–Arnold Networks (KAN) [30], which integrate adaptive spline representations into the network’s functional form. Each layer consists of a combination of a standard linear transformation with a base activation (e.g., SiLU), and a spline-based nonlinearity defined as:

$$\phi(x) = \lambda_0 \cdot \text{silu}(x) + \sum_{i=1}^{d+k-1} c_i B_i^d(x), \quad (5)$$

where,  $d$  is the spline order,  $k$  is the number of grid intervals,  $c_i, \lambda_0 \in \mathbb{R}$  are learnable parameters. In our case, we used B-splines with parameters  $d = 3$  (cubic splines) and  $k = 8$ . Thus, we had 10 basis functions. Each  $B_i^d(x)$  is defined recursively using the Cox-de Boor formula [31]:

$$B_i^d(x) = \frac{x - \xi_i}{\xi_{i+d} - \xi_i} B_i^{d-1}(x) + \frac{\xi_{i+d+1} - x}{\xi_{i+d+1} - \xi_{i+1}} B_{i+1}^{d-1}(x)$$

with the base case for  $d = 0$ :

$$B_i^0(x) = \begin{cases} 1, & \text{if } \xi_i \leq x < \xi_{i+1} \\ 0, & \text{otherwise} \end{cases}$$

where  $\{\xi_i\}$  are the knot points that define the spline, which is dynamically updated during training based on the distribution of input values.

Given three inputs,  $\mathbf{x} = (t, x, y) \in \mathbb{R}^3$ , the output of our network is computed as:

$$f(\mathbf{x}) = f(t, x, y) = \sum_{i=1}^{2n+1} \psi_i \left( \sum_{j=1}^n \phi_{ij}(x_j) \right), \quad (6)$$

where,  $n = 3$  is the input dimension,  $\psi_i : \mathbb{R} \rightarrow \mathbb{R}$  are the outer transformations, and  $\phi_{ij} : \mathbb{R} \rightarrow \mathbb{R}$  are the KAN activations applied to each input component.

Substituting for Eq. 5, Eq. 6 yields:

$$f(\mathbf{x}) = f_L \circ f_{L-1} \circ \dots \circ f_1(\mathbf{x})$$

where, each layer  $f_\ell$  applies the transformation:

$$f_\ell(\mathbf{z}) = \sum_{i=1}^{n_\ell} \left( \sum_{j=1}^{n_\ell-1} \left( \lambda_{ij}^{(0)} \cdot \text{silu}(z_j) + \sum_{r=1}^{g+d-1} c_{ijr} \cdot B_r^d(z_j) \right) \right)$$

with  $n_\ell$  being the number of neurons in layer  $\ell$ ,  $g$  being the grid size, and  $d$  being the spline order.

#### 4.4 Training Setup

To ensure a fair evaluation of the models, each model was trained for 60,000 iterations, using a decay step of 1,000 and a decay rate of 0.99. We employed PyTorch’s Adam optimizer with  $\beta_1 = 0.9$ ,  $\beta_2 = 0.999$ , and  $\epsilon = 10^{-8}$ . A Sobol sequence was used for the initial training dataset selection, and mini-batch gradient descent was performed with a batch size of 128, where samples were randomly selected from the Sobol-generated dataset to enhance model generalization. The training dataset included 0.005%, 0.05% of the fluid and solid interface data, respectively, ensuring efficient and representative sampling of boundary conditions and the solid interface. Furthermore, the training dataset and settings were standardized across all models to ensure a fair comparison and consistency in performance evaluation.

Finally, all experiments are performed on an NVIDIA A100 machine with a single node with 4 GPUs, each with 40 GB of VRAM. High-precision numerical solutions from Immersed Boundary Adaptive Mesh Refinement (IBAMR)

Table 3: The relative  $L_2$  error (in %) of the models (M1, M2, M3, and M2) considered in our study.

		Single-FSI		Eulerian-Lagrangian	
		M1↓	M2↓	M3↓	M4↓
Fluid	$u_x$	26.06	<b>13.2</b>	20.16	<b>11.78</b>
	$v_y$	23.56	<b>20.6</b>	15.15	<b>8.8</b>
	$p$	38.32	<b>30.5</b>	27.03	<b>17.68</b>
Solid interface	$u_x$	31.23	<b>6.09</b>	5.16	<b>1.41</b>
	$v_y$	19.28	<b>7.54</b>	2.92	<b>1.38</b>
	$p$	36.00	<b>21.31</b>	28.72	<b>13.08</b>

software are used as reference solutions. We evaluate the performance of the models using the relative  $L_2$ -norm, as follows:

$$\text{Relative } L_2 \text{ norm} = \frac{\|y - \hat{y}\|_2}{\|y\|_2} * 100\% \quad (7)$$

where,  $\hat{y}$  and  $y$  are the predicted and the reference solutions respectively.

## 5 Results and Discussion

We evaluated models M1, M2, M3, and M4 (see Fig. 2). This section presents relative error metrics, training convergence, and qualitative visualizations to comprehensively assess these models' performance.

### 5.1 Relative $L_2$ Error

Table 3 presents the relative  $L_2$  error (in %) for velocity and pressure predictions across both the fluid domain and solid interface for all four models. The Eulerian-Lagrangian models M3 and M4 consistently achieved lower relative  $L_2$  errors compared to Single-FSI models M1 and M2. This performance gap is particularly at the solid interface, where the specialized network design of the Eulerian-Lagrangian architecture demonstrates its effectiveness. Models using the adaptive B-spline activation, M2 and M4, consistently outperform their Tanh-based counterparts, M1 and M3. This trend is evident in both fluid domain and interface predictions.

### 5.2 Training Convergence

Fig. 4 illustrates the training loss curves over 60,000 epochs for all four evaluated models. Models employing B-spline activation, M2 and M4, demonstrate consistently faster convergence rates compared to their Tanh-based counterparts, M1 and M3. This acceleration is particularly noticeable in the early training phases (0 - 20,000 epochs), where B-spline models achieve steeper reduction in loss. Model M4 achieves the lowest final loss.

### 5.3 Reference vs. Prediction

Fig. 5 shows contour plots for model M2 (the best Single-FSI model) and model M4 (the best Eulerian-Lagrangian model), comparing them against the reference solution. The velocity components,  $u_x$  and  $u_y$ , show relatively smooth contours that closely align with the reference values across most of the domain. The pressure,  $p$ , distribution generally matches with the reference results, although there are significant discrepancies in certain regions, particularly near the fluid-solid interface.

Fig. 6 further illustrates the accuracy of the predictions through contour plots over time for our two best-performing models, M2 and M4. These plots track the Eulerian velocity components and pressure at key time steps (0, 1.0, 5.0, 6.0, 8.0, and 10.0 seconds). Model M2 shows larger deviations in velocity and pressure from the reference solution, especially at the initial time steps. Although the predictions gradually improve, discrepancies in the upper boundary region remain. In contrast, the model M4 captures the velocity and pressure profiles more accurately over time, closely matching the reference solution in shape and gradient distribution, particularly from time steps 5.0 onwards.

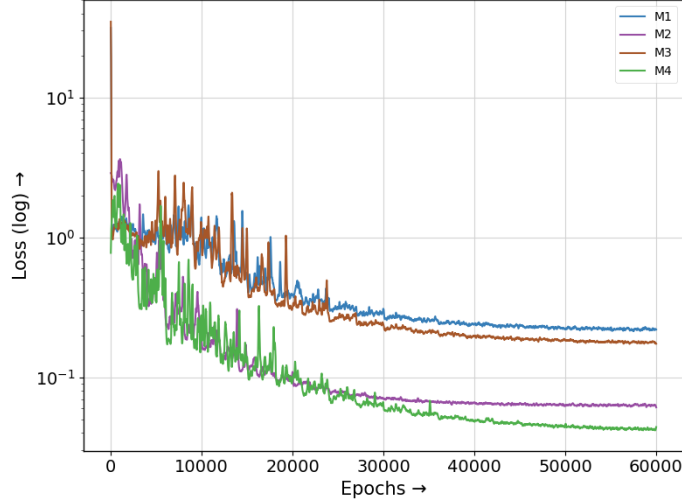


Figure 4: Training loss curves for the models (M1, M2, M3 and M4) over 60,000 epochs. The models correspond to the architectural and activation configurations detailed in Table 2.

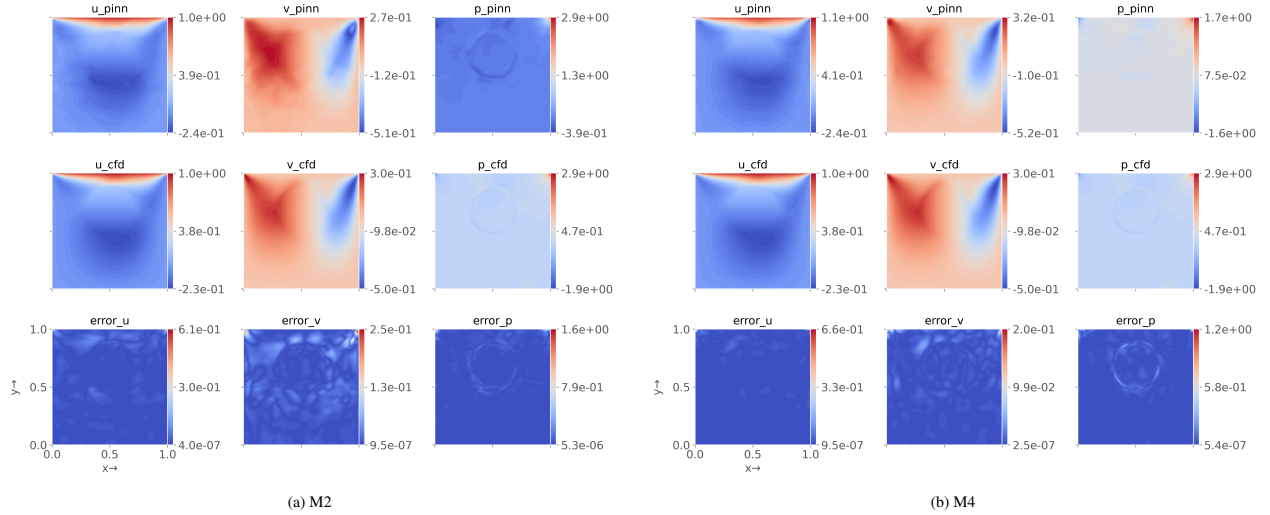


Figure 5: Contour plots for the solution of the FSI problem for the best-performing models (M2 and M4) derived from the Eulerian-Lagrangian network, illustrating the Eulerian velocities  $u_x$ ,  $v_y$  and the pressure  $p$  at steady state. The rows, from top to bottom, show the model-predicted solution, the reference CFD solution, and the point-wise absolute errors between the two solutions, respectively.

Additional results showing the agreement between models M2, M4, and the reference solution can be found in Appendix A.

## 5.4 Discussion

### 5.4.1 Limitation of single architecture approach

The Single-FSI architecture, which employs a unified network for the entire FSI domain, consistently faced difficulties with capturing abrupt variations at fluid-solid interfaces. As this approach treats both Eulerian and Lagrangian components uniformly, combining boundary conditions and PDE residuals through a single integrated loss function (Eq. 3a and Fig. 2). Our statistical analysis in Table 1 reveals substantial variability in target variables across domains, with particular disparity between fluid and interface regions. This heterogeneity poses a significant challenge for the Single-FSI network, as evidenced by the elevated error metrics in Table 3. The network’s shared parameter space is forced to simultaneously optimize for fundamentally different physical behaviors, leading to compromised performance

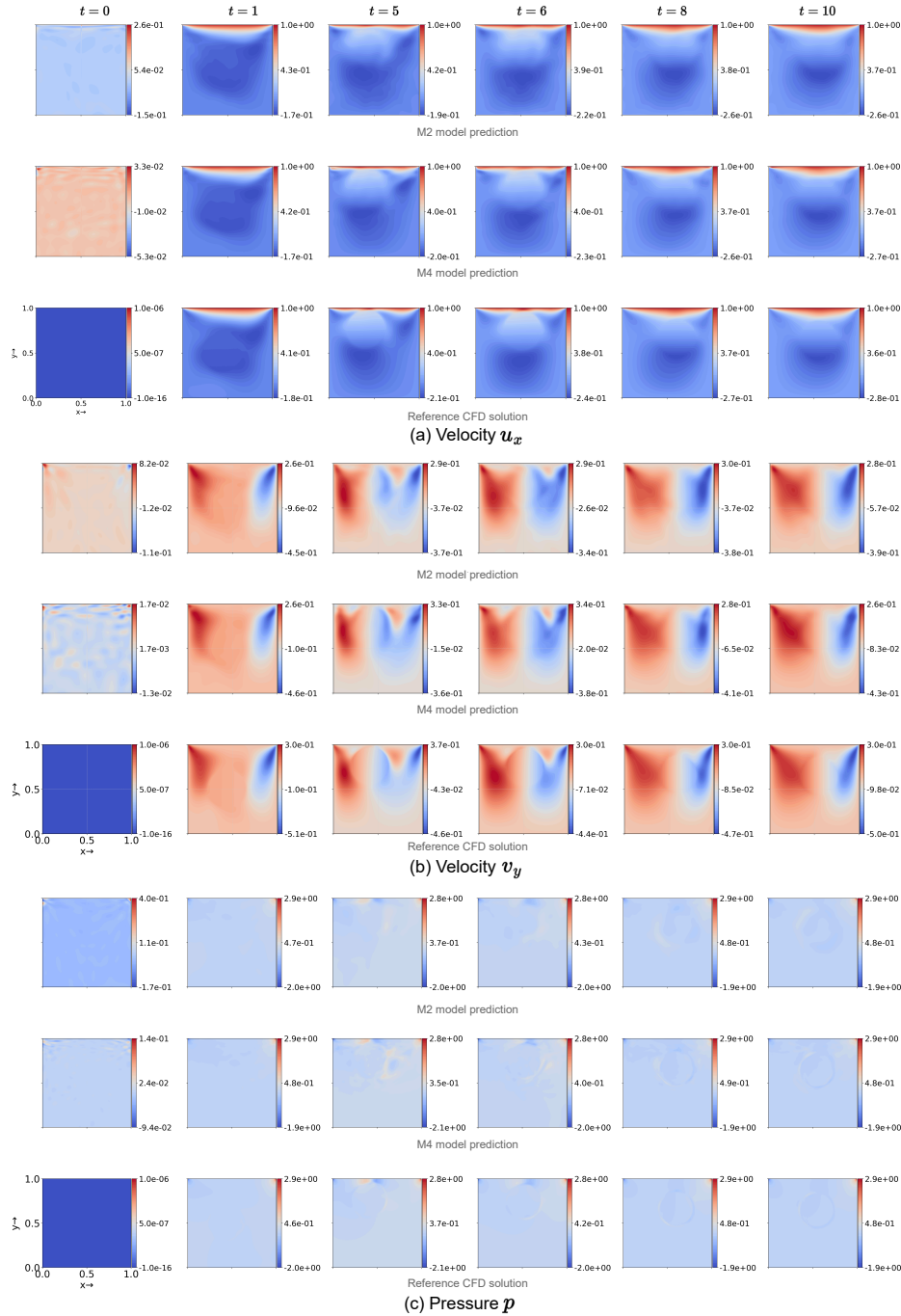


Figure 6: Comparison of the predictions from the best-performing models (M2 and M4) with the reference CFD solution for Eulerian velocities  $u_x$ ,  $v_y$ , and pressure  $p$  at various time steps (columns).

in both domains. These observations align with established findings in multi-task learning literature, where predicting multiple fields with distinct physical characteristics using a single network architecture leads to competing objectives due to parameter sharing across all predictions [22, 23, 24, 25]. The inherent tension between optimizing for fluid dynamics versus solid interface behavior creates a learning dilemma that cannot be adequately resolved within a unified parameter space.

### 5.4.2 Benefits of domain specialization

Our Eulerian-Lagrangian architecture addresses these limitations by decoupling the Eulerian and Lagrangian predictions into distinct specialized networks. This separation enables each network to focus exclusively on its respective domain-specific physics without interference from competing objectives. The fluid network can optimize for smooth, continuous flow fields governed by the Navier-Stokes equations, while the interface network can specialize in capturing the sharp gradients and boundary conditions characteristic of solid-fluid interfaces. This approach offers several key advantages over the Single-FSI architecture: (a) Each specialized network can accommodate the statistical distribution of its respective domain, reducing the impact of variable scaling issues during training. (b) Network capacity can be allocated more efficiently, with complexity distributed according to the specific modeling challenges of each domain. (c) The dedicated interface network can focus entirely on enforcing boundary conditions and capturing sharp transitions, leading to significantly more accurate velocity and pressure predictions at the critical fluid-solid boundary.

### 5.4.3 Complementary role of adaptive and fixed activation

Our experiments demonstrate that the adaptive B-spline basis function activation substantially outperforms standard Tanh activation in capturing localized, abrupt changes in flow properties. This improved performance arises from the activation function’s fundamental properties: (a) Unlike global activation functions, B-splines have compact support, allowing them to model sharp, localized features without affecting distant regions. (b) The learnable control points enable the network to automatically adjust representation capacity according to local complexity. (c) The hierarchical nature of B-splines naturally accommodates multi-scale phenomena, capturing both broad flow patterns and fine interface details.

Despite its limitations in capturing sharp interfaces, Tanh activation offers complementary strengths. Its smooth, global representation provides reliable convergence across the entire domain while effectively capturing broader flow patterns. The continuous, differentiable nature of Tanh makes it particularly suitable for regions dominated by gradual changes and continuous physics.

### 5.4.4 Loss weighting considerations and challenges

Beyond network architecture and activation functions, we explored various dynamic PINN loss-balancing schemes to enhance prediction accuracy. We experimented with several adaptive weighting methods: Gradient Statistics approach [32], Self-Adaptive (SA) method [33], and Residual-Based Attention (RBA) [34]. Contrary to expectations, none of these methods produced improved results. The gradient statistics method, in particular, encountered significant difficulties with “noisy” loss terms associated with coupling equations. These terms occasionally trained well in all models even under low gradient conditions, likely because they contain specific frequencies that are learned faster than others [35, 36]. The low gradients led the adaptive methods to assign larger weights to these terms, creating an imbalance that hindered convergence rather than improving it. This paradoxical behavior highlights the unique challenges of FSI problems, where such adaptive techniques developed for simpler physics problems may not transfer effectively. These challenges with traditional adaptive weighting reinforced our decision to focus on architectural improvements and activation function selection.

### 5.4.5 Implications for FSI modeling

The improved performance of our decoupled architecture with adaptive B-spline activations has significant implications for the broader field of FSI modeling: (a) **Architecture should reflect physical structure:** Our results demonstrate that neural network architecture should mirror the underlying physical structure of the problem domain, with specialized components for distinct physical regimes. (b) **Locality matters at interfaces:** The improvement from locality-aware activation functions underscores the critical importance of local representation capacity at fluid-structure interfaces. (c) **Adaptivity benefits are domain-specific:** While adaptive techniques are valuable, they must be tailored to FSI-specific challenges rather than applied as generic solutions from other domains.

## 6 Conclusion

In this paper, we developed and evaluated two neural network architectures within the IBM-PINN framework to address FSI problems: the Single-FSI architecture and the Eulerian-Lagrangian architecture. Each model was implemented with two activation function paradigms: standard Tanh and adaptive B-spline basis functions, resulting in four comprehensive models. We validated these approaches by solving the incompressible Navier-Stokes equations using 2D cavity flow with a moving solid structure inside. The models predict velocity and pressure fields across Eulerian fluid domains and Lagrangian solid interfaces.

We found a clear performance distinction between the architectural approaches. The Single-FSI architecture, which utilizes a unified network with shared parameters, consistently struggled to accurately capture sharp gradients and effectively enforce interface conditions. This limitation manifested in larger relative  $\mathcal{L}_2$  errors, highlighting the inherent challenges of managing competing objectives within a shared parameter space when modeling the distinct physics of fluid and solid domains. In contrast, the Eulerian-Lagrangian architecture improved prediction accuracy and more effectively captured the complex dynamics at fluid-solid interfaces. By dedicating specialized networks to each domain, this architecture enables learning of domain-specific dynamics and more precise modeling of interface exchanges without parameter interference.

Our evaluation of activation functions revealed complementary strengths and limitations. Models utilizing Tanh activation provided smooth global approximations with stable convergence properties during training. However, these models demonstrated limited capacity for handling localized high-gradient behavior, particularly near fluid-solid interfaces where rapid property changes occur. The adaptive B-spline activation function models exhibited better performance in capturing these sharp transitions. Their locality-aware properties enabled more precise representation of the abrupt changes in flow characteristics near boundaries, resulting in more accurate interface dynamics prediction. This finding validates our hypothesis that locality-aware representation techniques are particularly valuable for FSI problems.

Despite these advances, a few limitations remain in our approach. Training effectiveness continues to be significantly influenced by data quality and distribution, particularly around interface regions where physics complexity is highest. The relatively high  $\mathcal{L}_2$  error in pressure field prediction suggests that important physical interactions may not be adequately captured in our current learning objectives. We attribute this primarily to the omission of explicit force-coupling equations between fluid and interface domains. By focusing solely on enforcing velocity and pressure values without incorporating force equilibrium conditions, our models lack the necessary constraints to accurately resolve interfacial pressure and stress balance. To address these issues, future work should focus on enhancing physics integration by incorporating force-coupling equations directly into the loss function to better enforce interfacial momentum conservation. This should significantly improve pressure field predictions and overall accuracy.

## Acknowledgment

We thank the National Center for High-Performance Computing of Turkey (UHeM) for providing computing resources under grant number 5010662021.

## Funding

The first (AF) and last author (MSC) were funded by Bilimsel Araştırma Projeleri (BAP) under grant numbers 43019. The third (RD) and fourth (ECE) were funded by the Scientific and Technological Research Council of Turkey (TUBITAK) as part of the ARDEB 1001 program under grant numbers 120M671 and 124M416. The second author (SK) declares that no funds, grants, or other support were received during the preparation of this manuscript.

## Data Availability

All supporting code and data are included in the GitHub: [https://github.com/afrah/pinn\\_fsi\\_ibm](https://github.com/afrah/pinn_fsi_ibm)

## Author contributions

All authors read and approved the final manuscript.

**Keywords** Fluid Structure Interaction (FSI) · Immersed Boundary Method (IBM), · Physics Informed Neural Networks (PINN), · Activation

## References

- [1] Rajat Mittal and Gianluca Iaccarino. Immersed boundary methods. *Annual Review of Fluid Mechanics*, 37:239, 2005.

- [2] Boyce E Griffith, Xiaoyu Luo, David M McQueen, and Charles S Peskin. Simulating the fluid dynamics of natural and prosthetic heart valves using the immersed boundary method. *International Journal of Applied Mechanics*, 1(01):137–177, 2009.
- [3] Amneet P.S. Bhalla, Boyce E. Griffith, Neelesh A. Patankar, and Aleksandar Donev. A unified immersed boundary projection method for the incompressible navier–stokes equations. *Journal of Computational Physics*, 250:446–476, 2013.
- [4] Boyce E Griffith and Xiaoyu Luo. Hybrid finite difference/finite element immersed boundary method. *International journal for numerical methods in biomedical engineering*, 33(12):e2888, 2017.
- [5] Renkun Han, Yixing Wang, Weiqi Qian, Wenzheng Wang, Miao Zhang, and Gang Chen. Deep neural network based reduced-order model for fluid–structure interaction system. *Physics of Fluids*, 34(7), 2022.
- [6] Yangwei Liu, Shihang Zhao, Feitong Wang, and Yumeng Tang. A novel method for predicting fluid–structure interaction with large deformation based on masked deep neural network. *Physics of Fluids*, 36(2), 2024.
- [7] Wang Xiao, Ting Gao, Kai Liu, Jinqiao Duan, and Meng Zhao. Fourier neural operator based fluid–structure interaction for predicting the vesicle dynamics. *Physica D: Nonlinear Phenomena*, 463:134145, 2024.
- [8] Xiantao Fan and Jian-Xun Wang. Differentiable hybrid neural modeling for fluid-structure interaction. *Journal of Computational Physics*, 496:112584, 2024.
- [9] Farrukh Mazhar and Ali Javed. A new approach for spatio-temporal interface treatment in fluid–solid interaction using artificial neural networks employing coupled partitioned fluid–solid solvers. *Journal of Fluids and Structures*, 131:104200, 2024.
- [10] Rui Gao and Rajeev K Jaiman. Predicting fluid–structure interaction with graph neural networks. *Physics of Fluids*, 36(1), 2024.
- [11] Afrah Farea and Mustafa Serdar Celebi. Learnable activation functions in physics-informed neural networks for solving partial differential equations. *Computer Physics Communications*, page 109753, 2025.
- [12] Nan Li and Ming Wang. Data-driven localized waves of a nonlinear partial differential equation via transformation and physics-informed neural network. *Nonlinear Dynamics*, 113(3):2559–2568, 2025.
- [13] Yanjie Wang, Yaxin Peng, Zhaoping Hu, and Ying Li. Exploring prototype-guided strategy for domain decomposition in physics-informed neural network. *Nonlinear Dynamics*, pages 1–28, 2025.
- [14] Masaki Morimoto, Kai Fukami, Kai Zhang, and Koji Fukagata. Generalization techniques of neural networks for fluid flow estimation. *Neural Computing and Applications*, 34(5):3647–3669, 2022.
- [15] Saddam Hijazi, Melina Freitag, and Niels Landwehr. Pod-galerkin reduced order models and physics-informed neural networks for solving inverse problems for the navier–stokes equations. *Advanced Modeling and Simulation in Engineering Sciences*, 10(1):5, 2023.
- [16] Siddharth Nair, Timothy F Walsh, Greg Pickrell, and Fabio Semperlotti. Multiple scattering simulation via physics-informed neural networks. *Engineering with Computers*, pages 1–20, 2024.
- [17] Amirhassan Abbasi, Prashant N Kambali, Parham Shahidi, and C Nataraj. Physics-informed machine learning for modeling multidimensional dynamics. *Nonlinear Dynamics*, 112(24):21565–21585, 2024.
- [18] Hamid El Bahja, Jan C Hauffen, Peter Jung, Bubacarr Bah, and Issa Karambal. A physics-informed neural network framework for modeling obstacle-related equations. *Nonlinear Dynamics*, pages 1–12, 2025.
- [19] Rahul Sundar, Dipanjan Majumdar, Didier Lucor, and Sunetra Sarkar. Physics-informed neural networks modelling for systems with moving immersed boundaries: Application to an unsteady flow past a plunging foil. *Journal of Fluids and Structures*, 125:104066, 2024.
- [20] Dehong Fang and Jifu Tan. Immersed boundary-physics informed machine learning approach for fluid–solid coupling. 263:112360.
- [21] Yi Huang, Zhiyu Zhang, and Xing Zhang. A direct-forcing immersed boundary method for incompressible flows based on physics-informed neural network. *Fluids*, 7(2):56, 2022.
- [22] Ozan Sener and Vladlen Koltun. Multi-task learning as multi-objective optimization. *Advances in neural information processing systems*, 31, 2018.
- [23] Alex Kendall, Yarin Gal, and Roberto Cipolla. Multi-task learning using uncertainty to weigh losses for scene geometry and semantics. In *Proceedings of the IEEE conference on computer vision and pattern recognition*, pages 7482–7491, 2018.

- [24] Yin hao Zhu, Nicholas Zabaras, Pha edon-Stelios Koutsourelakis, and Paris Perdikaris. Physics-constrained deep learning for high-dimensional surrogate modeling and uncertainty quantification without labeled data. *Journal of Computational Physics*, 394:56–81, 2019.
- [25] Shengze Cai, Zhicheng Wang, Sifan Wang, Paris Perdikaris, and George Em Karniadakis. Physics-informed neural networks for heat transfer problems. *Journal of Heat Transfer*, 143(6):060801, 2021.
- [26] IBAMR Developers. IBAMR: An adaptive and distributed-memory parallel implementation of the immersed boundary method. <https://ibamr.github.io/>, 2024. Accessed: 2025-05-19.
- [27] Alessandra M Bavo, Giorgia Rocatello, Francesco Iannaccone, Joris Degroote, Jan Vierendeels, and Patrick Segers. Fluid-structure interaction simulation of prosthetic aortic valves: comparison between immersed boundary and arbitrary lagrangian-eulerian techniques for the mesh representation. *PloS one*, 11(4):e0154517, 2016.
- [28] Remco van der Meer, Cornelis W Oosterlee, and Anastasia Borovykh. Optimally weighted loss functions for solving pdes with neural networks. *Journal of Computational and Applied Mathematics*, 405:113887, 2022.
- [29] Shamsulhaq Basir. Investigating and mitigating failure modes in physics-informed neural networks (pinns). *Communications in Computational Physics*, 33(5):1240–1269, 2023.
- [30] Ziming Liu, Yixuan Wang, Sachin Vaidya, Fabian Ruele, James Halverson, Marin Soljačić, Thomas Y Hou, and Max Tegmark. Kan: Kolmogorov-arnold networks. *arXiv preprint arXiv:2404.19756*, 2024.
- [31] Carl De Boor. On calculating with b-splines. *Journal of Approximation theory*, 6(1):50–62, 1972.
- [32] Sifan Wang, Yujun Teng, and Paris Perdikaris. Understanding and Mitigating Gradient Flow Pathologies in Physics-Informed Neural Networks. *SIAM Journal on Scientific Computing*, 43(5):A3055–A3081, 2021.
- [33] Levi D McClenny and Ulisses M Braga-Neto. Self-adaptive physics-informed neural networks. *Journal of Computational Physics*, 474:111722, 2023.
- [34] Sokratis J Anagnostopoulos, Juan Diego Toscano, Nikolaos Stergiopoulos, and George Em Karniadakis. Residual-based attention in physics-informed neural networks. *Computer Methods in Applied Mechanics and Engineering*, 421:116805, 2024.
- [35] Nasim Rahaman, Aristide Baratin, Devansh Arpit, Felix Draxler, Min Lin, Fred Hamprecht, Yoshua Bengio, and Aaron Courville. On the spectral bias of neural networks. In *International conference on machine learning*, pages 5301–5310. PMLR, 2019.
- [36] Yuan Cao, Zhiying Fang, Yue Wu, Ding-Xuan Zhou, and Quanquan Gu. Towards understanding the spectral bias of deep learning. *arXiv preprint arXiv:1912.01198*, 2019.

## A Appendix

The plots in Fig. 7 to 9 show the predicted profiles of various fluid parameters along the x-axis across different randomly selected time steps with y-coordinates for models M2 and M4, compared to the reference solution.

The pressure is the most challenging variable to predict across all models. In contrast, velocity profiles are relatively easier for the models to capture. This discrepancy arises because the pressure components exhibit more pronounced discontinuities and abrupt changes than the velocity. In particular, the observed abrupt changes in the reference at points  $y = 0.89$  and  $y = 0.97$  likely indicate localized interactions at the solid interface.

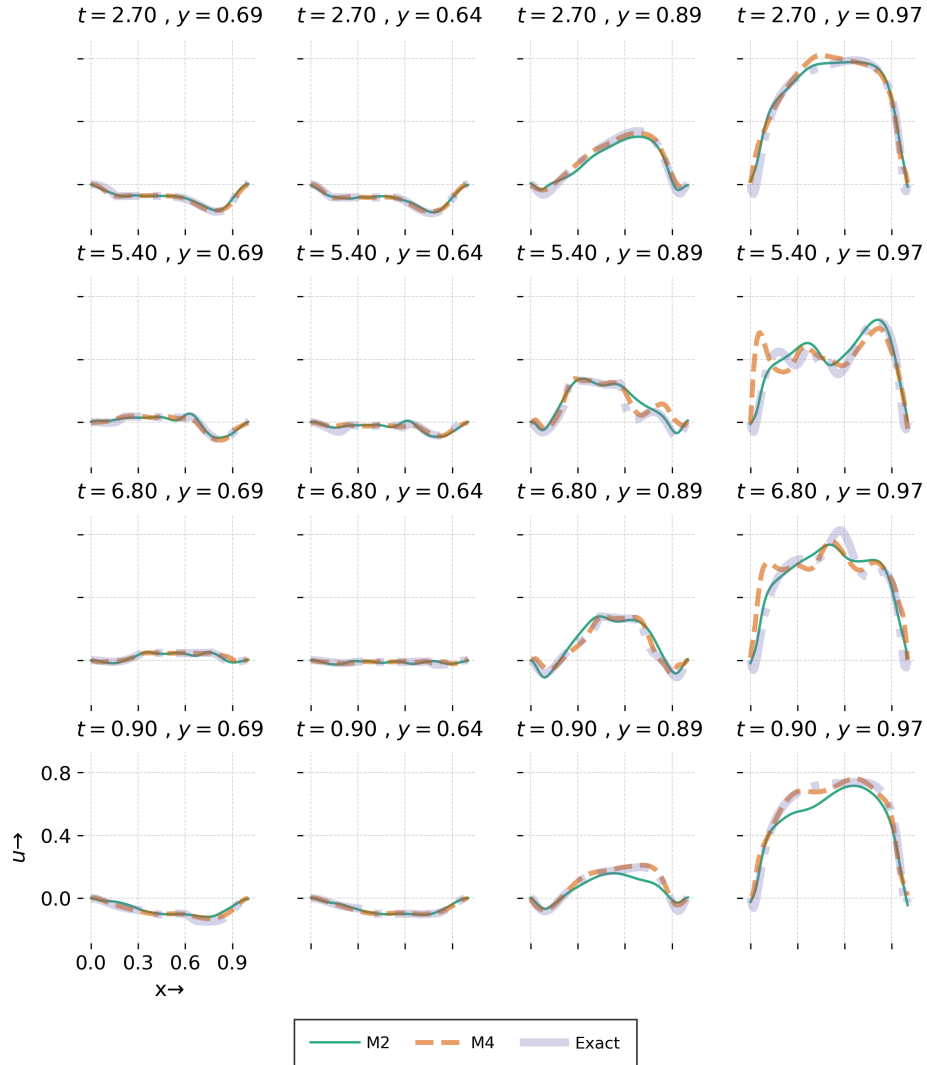


Figure 7: Predicted Eulerian velocity profiles  $u_x$  vs reference solution along the x-axis for different time steps and y-coordinates.

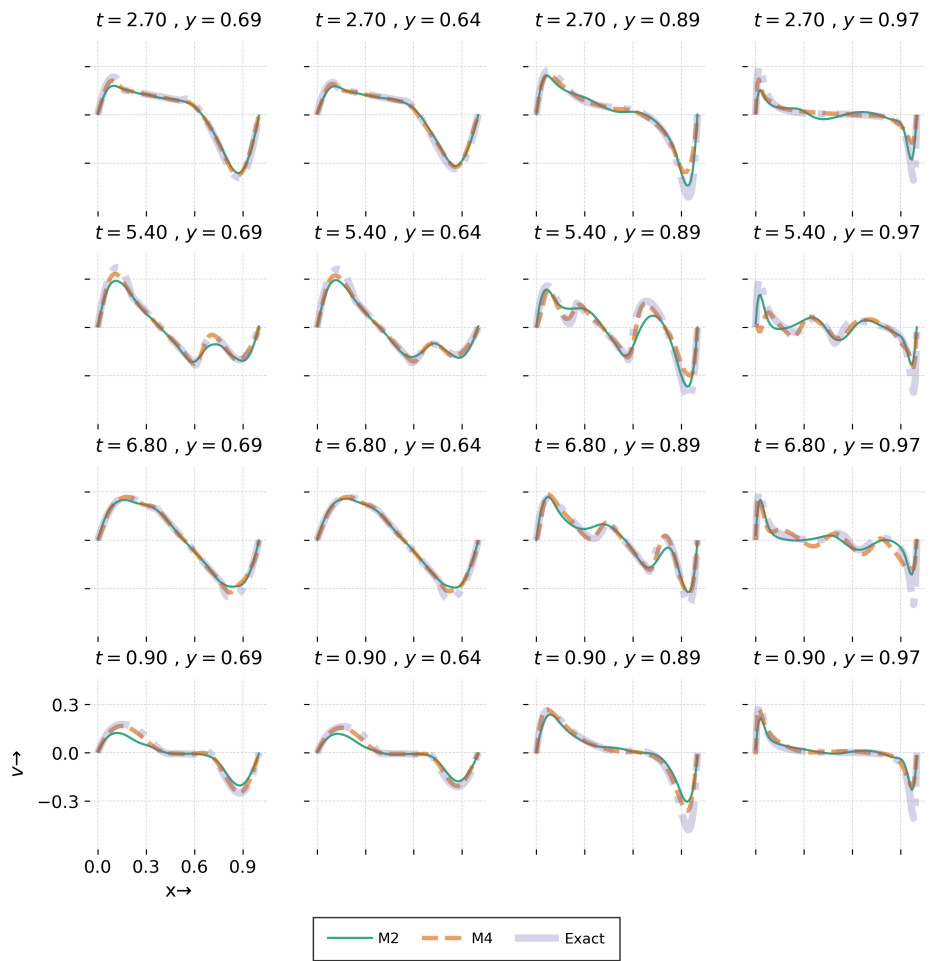


Figure 8: Predicted Eulerian velocity profiles  $v_y$  vs references solution along the x-axis for different time steps and y-coordinates.

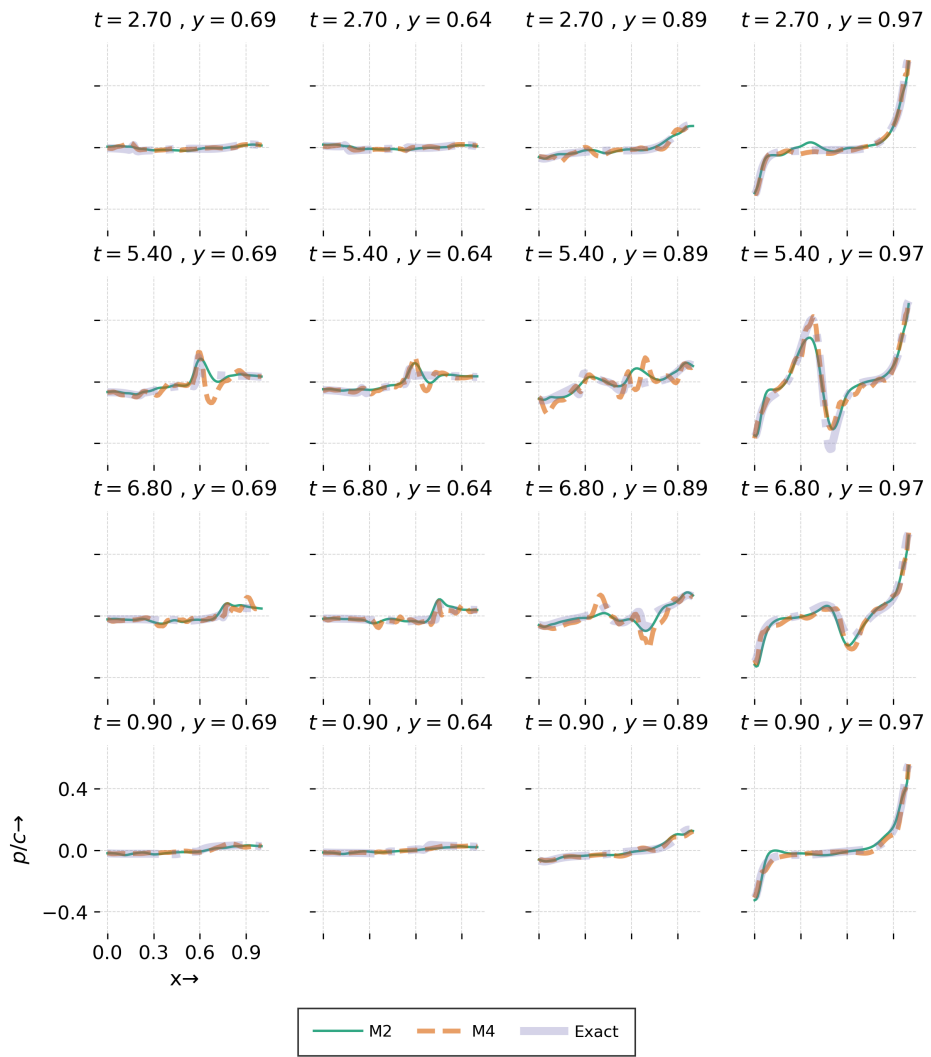


Figure 9: Pressure profiles  $p$  along the  $x$ -axis for different time steps and  $y$ -coordinates.